

Operando Tracking the Interactions between CoO_x and CeO_2 during Oxygen Evolution Reaction

Jinzhen Huang,* Natasha Hales, Adam H. Clark, Nur Sena Yüzbası, Camelia Nicoleta Borca, Thomas Huthwelker, Thomas J. Schmidt, and Emiliana Fabbri*

CeO_2 greatly enhances the electrocatalytic oxygen evolution reaction (OER) activity of CoO_x , though the enhancement mechanism beyond this synergy is yet to be understood. Here, operando hard X-ray absorption spectroscopy (hXAS) is applied to monitor the Co K edge and Ce L₃ edge in $\text{CoO}_x/\text{CeO}_2$ to shed light on the evolution of the Co and Ce oxidation states during OER. In addition, ex situ soft XAS (sXAS) characterizations provide information on the irreversible surface-specific transformations of the Co L₃ edge as well as of the O K edge. Combining the operando and ex situ spectroscopic characterizations with comprehensive electrochemical analyses, it is confirmed that CeO_2 is not the active center for the OER. However, coupling CeO_2 with CoO_x introduces significant modifications in the Co and O species at the CoO_x surface and alters the flat band potential (E_{fb}), leading to more favorable Co oxidation state transformations during OER and possibly modifying the preferential reaction pathway. This work establishes the connections between electronic structures, Co oxidation state and the OER reaction mechanism for $\text{CoO}_x/\text{CeO}_2$ composites electrodes.

However, the OER performance of some catalysts is limited by the lack of active sites or poor conductivity. Therefore, creating nanocomposites to exploit the beneficial effects of synergistic interactions is an important strategy for improving the OER activity of these materials.^[4] In particular, CeO_2 has fast and reversible redox properties, good oxygen conductivity, and storage capabilities, as well as good proton conduction in some specific conditions.^[5] Coupling CeO_2 with other transition-metal-based electrocatalysts can improve their electrocatalytic performance in various reactions (including OER, hydrogen evolution/oxidation reaction, CO_2 reduction and, so on).^[6] For example, a surface CeO_x layer enhances the OER stability of NiFeO_x , since its permselectivity prevents the dissolution of Fe into the electrolyte.^[6c] Moreover, the electronic interactions between

CeO_2 and Co_3O_4 could modulate the Co redox to reduce the overpotential without increasing the Co dissolution during OER in an acidic environment, thus mitigating the activity/stability trade-off.^[6b]

However, even though it is widely recognized that coupling CeO_2 with Co-based materials can improve the OER performance of Co-based catalysts,^[7] the mechanism behind this improvement in performance is still under debate due to lack of comprehensive characterizations. For example, Kim et al.^[7a] proposed that doping Ce could promote the formation of CoOOH in CoO_x

1. Introduction

Water electrolysis powered by renewable electricity is one of the most promising means to achieve sustainable, carbon-neutral long-term energy storage in the form of hydrogen in a multi-energy carrier energy system.^[1] Recently, alkaline water splitting has attracted increasing interest, with rapid progression in the development on anion exchange membrane, electrocatalysts, and devices.^[2] The alkaline environment enables the application of transition-metal-based oxides as cost-effective OER catalysts.^[3]

J. Huang, N. Hales, T. J. Schmidt, E. Fabbri
Electrochemistry Laboratory
Paul Scherrer Institut
Villigen PSI CH-5232, Switzerland
E-mail: jinzhen.huang@psi.ch; emiliana.fabbri@psi.ch

A. H. Clark, C. N. Borca, T. Huthwelker
Photon Science Division
Paul Scherrer Institute
Villigen PSI CH-5232, Switzerland
N. S. Yüzbası
Laboratory for High Performance Ceramics
Empa – Swiss Federal Laboratories for Materials Science and Technology
Dübendorf CH-8600, Switzerland
T. J. Schmidt
Institute for Physical Molecular Sciences
ETH Zürich, Zürich CH-8093, Switzerland

The ORCID identification number(s) for the author(s) of this article can be found under <https://doi.org/10.1002/aenm.202303529>

© 2024 The Authors. Advanced Energy Materials published by Wiley-VCH GmbH. This is an open access article under the terms of the [Creative Commons Attribution](#) License, which permits use, distribution and reproduction in any medium, provided the original work is properly cited.

DOI: 10.1002/aenm.202303529

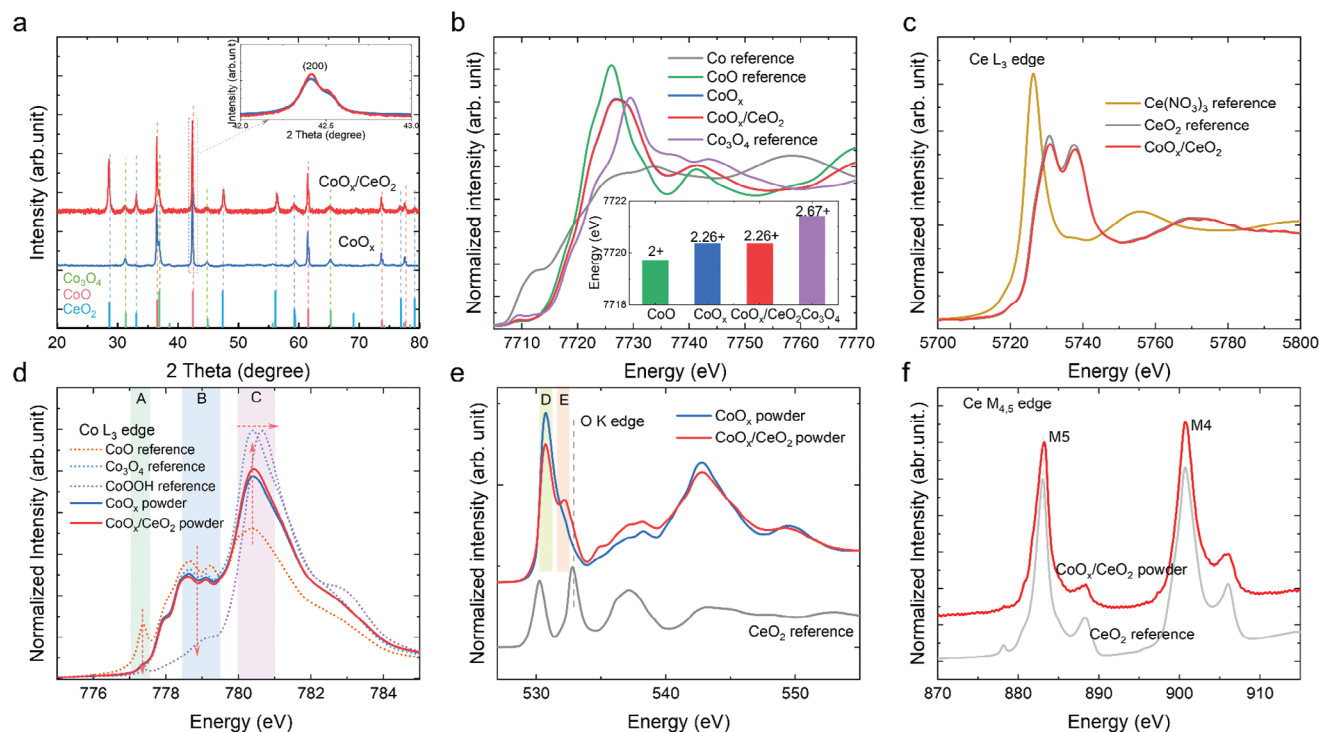


Figure 1. Structural characterizations on CoO_x and $\text{CoO}_x/\text{CeO}_2$. a) XRD patterns; inset shows the CoO (002) peak. b) XANES spectra at the Co K edge; inset shows the E_{edge} of different samples. c) XANES spectra at the Ce L_3 edge. The sXAS spectra at the d) Co L_3 edge, e) O K edge, and f) Ce $M_{4,5}$ edge.

and optimize the binding energy of OER intermediates. Qiu et al.^[7b] suggested the built-in electron field in the $\text{Co}_3\text{O}_4/\text{CeO}_2$ p-n heterojunction can reduce the Co^{III} to Co^{II} in the octahedral site and produce oxygen vacancies. In comparison, Liu et al.^[7c] suggested there was also a high concentration of oxygen vacancies at the $\text{Co}_3\text{O}_4/\text{CeO}_2$ interface; however, rather than Co^{III} being reduced, Ce^{IV} was reduced to Ce^{III} to facilitate the electron transfer. Moreover, Li et al.^[7d] proposed the Ce donated more electron to the lattice oxygen to reinforce the $\text{Co}-\text{O}$ covalency. Overall, even though different interaction mechanisms have been proposed, little attention has been paid to the interactions between Co and Ce during the OER due to the lack of operando characterizations. Besides, the role of lattice oxygen should be verified, since oxygen vacancies are suggested to play an important role in determining the OER activity.^[3c,8] Systematically linking structural properties, electronic features and electrochemical behavior is helpful to reach a more comprehensive understanding of the nature of $\text{Co}-\text{Ce}$ interactions and subsequent enhancement of the OER activity.

Herein, using the advantages of operando hXAS characterizations at the Co K edge and Ce L_3 edge, we are able to monitor the evolution of both CoO_x and CeO_2 in a $\text{CoO}_x/\text{CeO}_2$ nanocomposite during OER. We confirm that the Ce oxidation state does not change with increasing potential in the OER region, thus it is not the active center. Conversely, the Co oxidation state in $\text{CoO}_x/\text{CeO}_2$ responds clearly to the applied potential but behaves differently compared to CoO_x without CeO_2 . With the help of ex situ sXAS and in situ impedance spectroscopic characterizations, we confirm the interactions between CeO_2 and CoO_x could trigger a modification of both structural and electronic material charac-

teristics. Finally, investigation of the pH-dependence of the OER activity shows that CoO_x and $\text{CoO}_x/\text{CeO}_2$ have different reaction orders, indicating that proton and electron transfer during the rate-determining step (RDS) may be also altered due to interactions between CoO_x and CeO_2 .

2. Results and Discussion

The CoO_x and $\text{CoO}_x/\text{CeO}_2$ have been synthesized via flame spray pyrolysis, following a similar protocol developed in our group previously (see Experimental Section, Supporting Information, for more details).^[3a] The structural properties of the as-prepared catalysts were verified by X-ray diffraction (XRD), as shown in Figure 1a. The CoO_x sample is composed of CoO and Co_3O_4 . When 10% (molar ratio) of Ce is introduced during synthesis, there is no obvious shift in the XRD peaks; rather, CeO_2 is present as a separate phase, thus the sample is denoted as $\text{CoO}_x/\text{CeO}_2$. Other control samples with different $\text{Ce}/(\text{Ce}+\text{Co})$ percentages have also been synthesized following similar protocol for comparison (Figure S1, Supporting Information).

Furthermore, the ex situ hXAS was applied to understand the Co oxidation state and the electronic structure of the as-prepared catalysts. The X-ray absorption near edge spectroscopy (XANES) spectra at the Co K edge for both CoO_x and $\text{CoO}_x/\text{CeO}_2$ are almost overlapping, suggesting no significant difference in the average Co oxidation state (Figure 1b). The energy of the absorption edge (E_{edge}) was determined by using either an integration method^[6b,9] (inset in Figure 1b) or the energy at half (0.5 in arbitrary units) of the normalized edge jump^[10] (Figure S2a, Supporting Information), obtaining almost identical trend among the

samples. Furthermore, the E_{edge} values for both CoO_x and $\text{CoO}_x/\text{CeO}_2$ sit between the reference CoO and Co_3O_4 samples, with the Co oxidation of around 2.26+ from linear regression (Figure S2b, Supporting Information), as would be expected in a composite of CoO and Co_3O_4 . Therefore, the Fourier transform (FT) of the Co K edge extended X-ray absorption fine structure (EXAFS) shows the combining features of CoO and Co_3O_4 structures for both single material CoO_x and $\text{CoO}_x/\text{CeO}_2$ composite electrode (Figure S3a, Supporting Information). The Ce oxidation state in the $\text{CoO}_x/\text{CeO}_2$ was identified from the Ce L₃ edge spectrum, using $\text{Ce}(\text{NO}_3)_3$ and CeO_2 as references (Figure 1c). The XANES spectrum, and the corresponding FT-EXAFS spectrum (Figure S3b, Supporting Information) of Ce L₃ edge in $\text{CoO}_x/\text{CeO}_2$ are similar to those of the CeO_2 reference, proving that the Ce in the composite exists as the fluorite CeO_2 structure.

Since the OER is a surface process, the surface oxidation state of the catalyst will strongly relate to its catalytic performance. The sXAS combined with surface-sensitive total electron yield detection was used to study the Co L edge, O K edge, and Ce M edge of CoO_x and $\text{CoO}_x/\text{CeO}_2$ (Figure 1d–f). The full spectra for the Co L edge are shown in Figure S4 (Supporting Information), while the Co L₃ edge is highlighted in Figure 1d to demonstrate the Co oxidation state at the surface. The peaks, from low to high absorption energy, are attributed to octahedral Co^{II} (≈ 722 eV, in region A), tetrahedral/octahedral Co^{II} (≈ 779 eV, in region B) and Co^{III} (≈ 780 eV, in region C), respectively.^[11] The arrows in Figure 1d shows the trend of peak shift in different regions with increasing Co oxidation. Clearly, the peak intensity for both CoO_x and $\text{CoO}_x/\text{CeO}_2$ is greatly reduced in region A compared to that of reference CoO . Generally, the as-prepared CoO_x from flame spray synthesis show a Co_3O_4 -like surface. They overlap with reference Co_3O_4 in region B, however, the peaks have lower intensity in region C. These results are consistent with the trend in average Co oxidation state observed in the Co K edge from hXAS. The peak of $\text{CoO}_x/\text{CeO}_2$ in region C is slightly higher than that of CoO_x , indicating a higher fraction of Co^{III} species are present on its surface. Furthermore, O K edge was probed to reveal the orbital hybridization between Co 3d and O 2p (Figure 1e). The pre-edge resonance at ≈ 530.7 eV (in region D) is attributed to the Co^{III} –O hybridized state, while the one at ≈ 532 eV (in region E) is suggested to be the protonated bridging oxygen that adsorbs at defective sites (e.g., corner, edge and metal vacancy sites).^[11,12] To find out the contribution of CeO_2 to the O K edge, a CeO_2 reference sample has also measured (Figure 1f). The peak at ≈ 533 eV in the reference CeO_2 , due to the hybridization between O 2p and Ce 5d- e_g orbitals,^[13] does not overlap with peak assigned to the protonated bridging oxygen in $\text{CoO}_x/\text{CeO}_2$, which suggests this interested peak is not directly contributed from the CeO_2 in the composite. Furthermore, the surface-sensitive sXAS results revealed no obvious shift in the Ce M edge of $\text{CoO}_x/\text{CeO}_2$ compared to the reference CeO_2 , further proving that Ce is majorly present in the 4+ (Figure 1f). In general, the sXAS results indicate the interactions between CoO_x and CeO_2 endow the $\text{CoO}_x/\text{CeO}_2$ composite with a defective surface, potentially leading to improved OER performance.

To evaluate the OER activity, cyclic voltammetry (CV) was conducted in 0.1 M KOH to investigate the Co redox properties and the OER current in CoO_x and $\text{CoO}_x/\text{CeO}_2$ (Figure 2a). Typically, there are two pairs of redox peaks in both samples, which are at-

tributed to $\text{Co}^{\text{II/III}}$ and $\text{Co}^{\text{III/IV}}$, at ≈ 1.21 V and 1.48 V versus RHE, respectively.^[14] The $\text{CoO}_x/\text{CeO}_2$ shows more prominent $\text{Co}^{\text{III/IV}}$ redox peaks and a reduced overpotential for OER. To exclude impacts from the pseudocapacitive current attributed from Co redox processes, a steady-state chronoamperometric (CA) technique was applied to obtain the polarization curve for OER (Figure S5, Supporting Information). The $\text{CoO}_x/\text{CeO}_2$ still shows earlier onset and thus has improved OER activity. Compared to CoO_x , the mass activity of $\text{CoO}_x/\text{CeO}_2$ at 1.55 V versus RHE is remarkably enhanced (≈ 12.6 time higher), and at a current density of 10 A g^{-1} the overpotential is 40 mV lower (Figure 2b). The control samples synthesized with different percentages of Ce have also been investigated (Figure S6, Supporting Information). The $\text{CoO}_x/\text{CeO}_2$ with 10% Ce, the focus of this work, shows the best OER performance; nevertheless, also the composite samples with Ce in the 2–30% range outperform CoO_x in the OER activity. Therefore, adding an optimized amount of CeO_2 to CoO_x brings simultaneously two major advantages: it allows the amount of Co, whose price is constantly increasing, to be reduced and the OER activity to be increased. Furthermore, the control samples of physical mixing of CeO_2 with CoO_x (or Co_3O_4) do not show improved OER activity (Figure S7, Supporting Information), suggesting that the establishment of interactions at the interface of CoO_x and CeO_2 particles is crucial to induce the synergy between the two phases in the $\text{CoO}_x/\text{CeO}_2$ composite. A possible O-bridged interaction between Co and Ce at the interface may yield an improved absorption strength of OER intermediates, leading to improved OER activity.^[15]

We further verify the contributions of surface area and conductivity to the improved OER performance of $\text{CoO}_x/\text{CeO}_2$. The surface areas of the catalysts were estimated by two different methods (Figure 2c; Figure S8, Supporting Information). The Brunauer–Emmett–Teller (BET) surface area of $\text{CoO}_x/\text{CeO}_2$ ($\approx 28.4 \text{ m}^2 \text{ g}^{-1}$) is only slightly higher than that of CoO_x ($\approx 26.0 \text{ m}^2 \text{ g}^{-1}$). Nevertheless, $\text{CoO}_x/\text{CeO}_2$ shows higher specific activity, whether normalized by BET surface area or double layer capacitance (C_{dl}) (Figure S9, Supporting Information). The double layer capacitance (C_{dl}), extracted from the CVs at different scan rates (Figure S8c, Supporting Information), is smaller for the $\text{CoO}_x/\text{CeO}_2$ ($\approx 0.79 \text{ mF g}^{-1}$) compared to CoO_x ($\approx 1.43 \text{ mF g}^{-1}$), due to the contribution from CeO_2 . Four-wire impedance spectroscopy^[16] was conducted to show that the ex situ electron conductivity of CoO_x and $\text{CoO}_x/\text{CeO}_2$ is on the same order of magnitude ($10^{-6} \text{ S cm}^{-1}$) (Figure 2d), proving the adding CeO_2 does not hamper electron transfer among the particles. Besides, according to electrochemical impedance spectroscopy (EIS) measurements at 1.60 V versus RHE, $\text{CoO}_x/\text{CeO}_2$ shows better electrode kinetics with a smaller electron transfer resistance of $\approx 87.9 \text{ ohm}$ at 1.60 V versus RHE compared to $\approx 270.5 \text{ ohm}$ for CoO_x (Figure 2d; Figure S10, Supporting Information), in agreement with OER activity measurements. In all, combining CeO_2 with CoO_x improves the intrinsic OER activity.

To understand how the synergy between CoO_x and CeO_2 enhances the OER activity, ex situ sXAS characterizations in total electron yield (TEY) mode have been used to monitor the evolution of the Co L₃ edge and O K edge before and after the OER. The Co L₃ edge of dropcasted CoO_x and $\text{CoO}_x/\text{CeO}_2$ (i.e., before the OER) and after the OER were compared to that of the as-synthesized powder (Figure 3a,b). The major changes happening

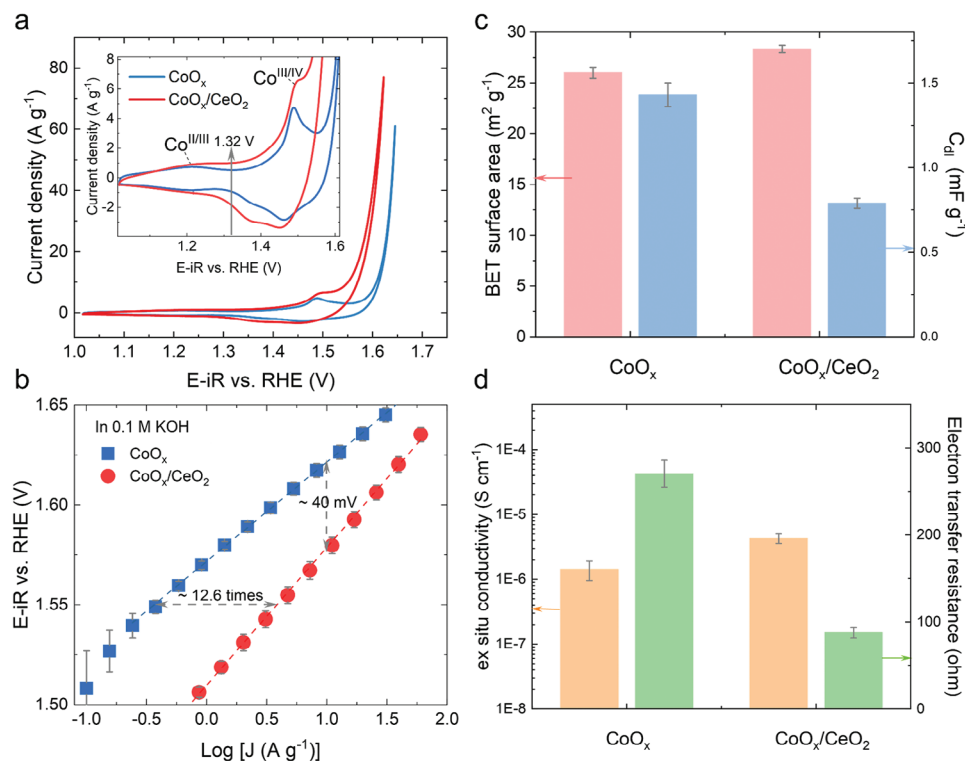


Figure 2. Electrochemical characterizations on CoO_x and $\text{CoO}_x/\text{CeO}_2$. a) CVs collected in 0.1 M of KOH, with a scan rate of 50 mV s^{-1} . The inset highlights the $\text{Co}^{\text{III/IV}}$ and $\text{Co}^{\text{III/IV}}$ redox pairs. b) Tafel plots obtained by CA measurement; the error bars are from the averages on three individual measurements. c) BET surface area calculated from N_2 absorption isotherm curves and C_{dl} ; the error bars are from fitting. d) Ex situ conductivity extracted from four-wire impedance spectroscopy and electron transfer resistance obtained by EIS measurement at 1.60 V versus RHE; the error bars are from the averages on three individual measurements and the fitting, respectively.

in region C correlate to the formation of octahedral Co^{III} . To better present the differences between CoO_x and $\text{CoO}_x/\text{CeO}_2$, the peak intensity ratio between region C and B (denoted as $I_{\text{C}}/I_{\text{B}}$) was calculated (insets in Figure 3a,b). $\text{CoO}_x/\text{CeO}_2$ powder has a slightly higher $I_{\text{C}}/I_{\text{B}}$ compared to CoO_x powder (≈ 2.05 versus 1.93), suggesting there is an initially higher Co oxidation state on the surface. The dropcasted samples, in which the catalyst makes contact with water during ink preparation, see an $I_{\text{C}}/I_{\text{B}}$ increase of ≈ 0.12 and 0.05 for CoO_x and $\text{CoO}_x/\text{CeO}_2$, respectively. It is reported that a transition from rocksalt CoO into Co_3O_4 will happen under open circuit potential.^[17] The changes in Co L_3 edge indicates there is chemical reconstruction during electrode preparation, and it is more significant for the CoO_x . The $I_{\text{C}}/I_{\text{B}}$ is further increased after the OER for both CoO_x and $\text{CoO}_x/\text{CeO}_2$, suggesting a higher fraction of Co^{III} is generated. Moreover, the discrepancy in surface oxidation between CoO_x and $\text{CoO}_x/\text{CeO}_2$ is more obvious in the O K edge spectra (Figure 3c,d). Similarly, the peak intensity ratio between regions E and D (denoted as $I_{\text{E}}/I_{\text{D}}$) has been calculated, with $I_{\text{E}}/I_{\text{D}} = \approx 0.34$ for the Co_3O_4 reference (Figure S11, Supporting Information). Clearly, the $I_{\text{E}}/I_{\text{D}}$ of CoO_x is similar to that of the Co_3O_4 reference under all conditions (i.e., as-synthesized powder, before the OER, after the OER) (inset in Figure 3c). Conversely, the $I_{\text{E}}/I_{\text{D}}$ of $\text{CoO}_x/\text{CeO}_2$ is much larger than 0.34 under all three conditions, suggesting a higher fraction of the protonated bridging oxygen is present at the defective surface sites. Notably, the $I_{\text{E}}/I_{\text{D}}$ of $\text{CoO}_x/\text{CeO}_2$ reached

≈ 1.09 after contacting with water and before the OER and was decreased down at ≈ 0.55 after the OER (inset in Figure 3d). Therefore, it is evident that the interactions between CoO_x and CeO_2 in $\text{CoO}_x/\text{CeO}_2$ modulate the electronic structure and surface Co oxidation state of the composite during the electrocatalytic process. Usually, the OCP of a material is related to its electronic structure.^[18] As the OCP of $\text{CoO}_x/\text{CeO}_2$ is 110 mV higher than that of CoO_x , this confirms that a modulation in electronic structure is induced by CeO_2 (Figure S12, Supporting Information).

Operando hXAS characterizations of the Co K edge and Ce L_3 edge were performed to track the interactions between CoO_x and CeO_2 during the OER (Figure 4). The hXAS spectra acquisition has a time-resolution of two spectra per second, thus enabling the capture of energy shifts in the E_{edge} during CV measurements with a slow scan rate of 2 mV s^{-1} . To better present the results, the 20 spectra collected every 10 s are averaged to have the resolution of 20 mV at the applied potential. The applied potential window for each operando measurement has been optimized by limiting the maximum current density to avoid gas bubbles formation impeding the quality of the XAS data obtained. Due to the higher activity of the $\text{CoO}_x/\text{CeO}_2$ composite, the upper applied potential used was reduced from 1.63 to 1.6 V (Figure S13, Supporting Information). The XANES spectra of the Co K edge for both CoO_x and $\text{CoO}_x/\text{CeO}_2$ shift to higher energy with increasing applied potential, due to the oxidation of Co (Figure 4a,b). To specify, the energy of E_{edge} was determined by the integration

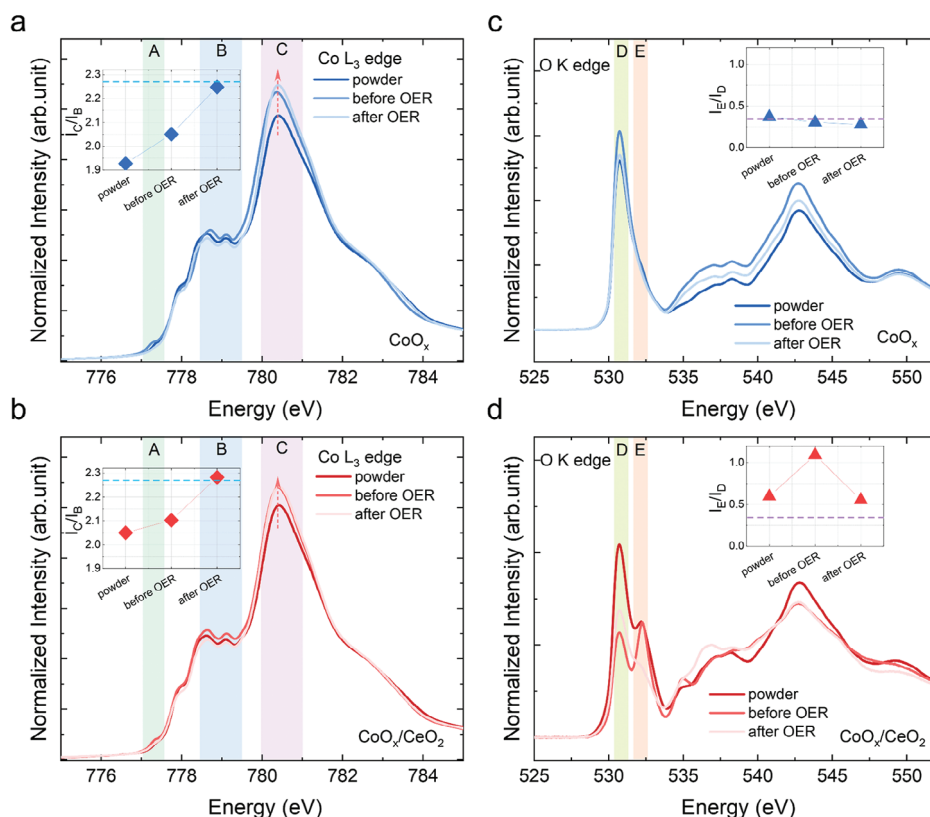


Figure 3. Ex situ xSAS characterizations (in TEY mode) on CoO_x and $\text{CoO}_x/\text{CeO}_2$ to compare the Co L_3 edge and O K edge of powder to those before OER (prepared in the catalyst ink and dropcasted on glassy carbon) and after OER. The Co L_3 edge spectra of a) CoO_x and b) $\text{CoO}_x/\text{CeO}_2$; the insets display the corresponding peak intensity ratio between region C and B (I_C/I_B) at the Co L_3 edge, with the dash line at 2.27 from Co_3O_4 reference for comparison. The O K edge of c) CoO_x and d) $\text{CoO}_x/\text{CeO}_2$; the insets display the corresponding peak intensity ratio between region E and D (I_E/I_D) in the O K edge, with the dash line at 0.34 from Co_3O_4 reference for comparison.

method outlined earlier.^[6b,9] The energy shift (ΔE_{edge}), representing the change in Co oxidation state, is obtained by comparing the E_{edge} at a specific applied potential to that seen at a potential of 1.0 V versus RHE during the first anodic scan. Taking the data for the first anodic scan as an example, the ΔE_{edge} of CoO_x increased continuously with the applied potential from 1.0 to 1.63 V versus RHE, whereas the ΔE_{edge} of $\text{CoO}_x/\text{CeO}_2$ showed a bi-phasic tendency, growing slowly before the $\text{Co}^{\text{III/IV}}$ redox peaks (≈ 1.32 V vs RHE in Figure 2a) but increasing steeply after that (Figure S14, Supporting Information). The ΔE_{edge} of $\text{CoO}_x/\text{CeO}_2$ before the $\text{Co}^{\text{III/IV}}$ redox peaks is only ≈ 10 meV, in contrast to ≈ 30 meV for CoO_x . The increase of Co oxidation state (i.e., ΔE_{edge}) before the OER can be correlated to surface deprotonation.^[14,19]

A total of 10 CV cycles were measured by scanning the potential forth and back (Figure 4d), to verify the reversibility of the Co oxidation state in CoO_x (Figure 4e). The ΔE_{edge} of CoO_x overlaps in the first anodic and cathodic scan, and there are no obvious changes even after 10 cycles (Figure 4e); the ΔE_{edge} of the Co foil used as a reference show no obvious periodic changes (Figure S15, Supporting Information), excluding the influence from the beam and other setups. In comparison, the ΔE_{edge} of $\text{CoO}_x/\text{CeO}_2$ shows an increase of ≈ 27 meV (indicated as the green dashed arrow in Figure 4f) as the potential is decreased from 1.6 to 1.0 V versus RHE at the end of the tenth cycle. This is most likely

due to partial irreversible oxidation of Co^{II} into Co^{III} during OER for $\text{CoO}_x/\text{CeO}_2$, as already observed in other Co-based catalysts.^[10b,20] Indeed, the reversibility of Co oxidation is slightly modified by the formation of the $\text{CoO}_x/\text{CeO}_2$ composite.

The periodic change of Co K edge showing a slight change E_{edge} indicates that Co is the active center for OER (Figure 4e,f). The reproducible and reversible small change in the Co K edge is additionally demonstrated through multivariate analysis (Figure S16, Supporting Information). In comparison, the evolution of the Ce oxidation state was monitored via the Ce L_3 edge spectra, with no apparent changes in the E_{edge} for Ce L_3 edge with the applied potential over the whole 10 CV cycles (Figure 4g). A similar trend has also been detected for the single phase CeO_2 reference material, which is inactive toward OER (Figure S6, Supporting Information), clearly showing that Ce is not redox-active during OER (Figure S17, Supporting Information). Thus far, we can safely conclude that CeO_2 does not directly participate in the OER as an active site.

After operando tracking of the Co oxidation state during CV, we have further conducted steady-state chronopotentiometry (CP) measurements (Figures S18 and S19, Supporting Information). The ΔE_{edge} (i.e., the change in Co oxidation state) has been plotted as the function of both the applied potential and the logarithm of current density (Figure 5a,b). The ΔE_{edge}

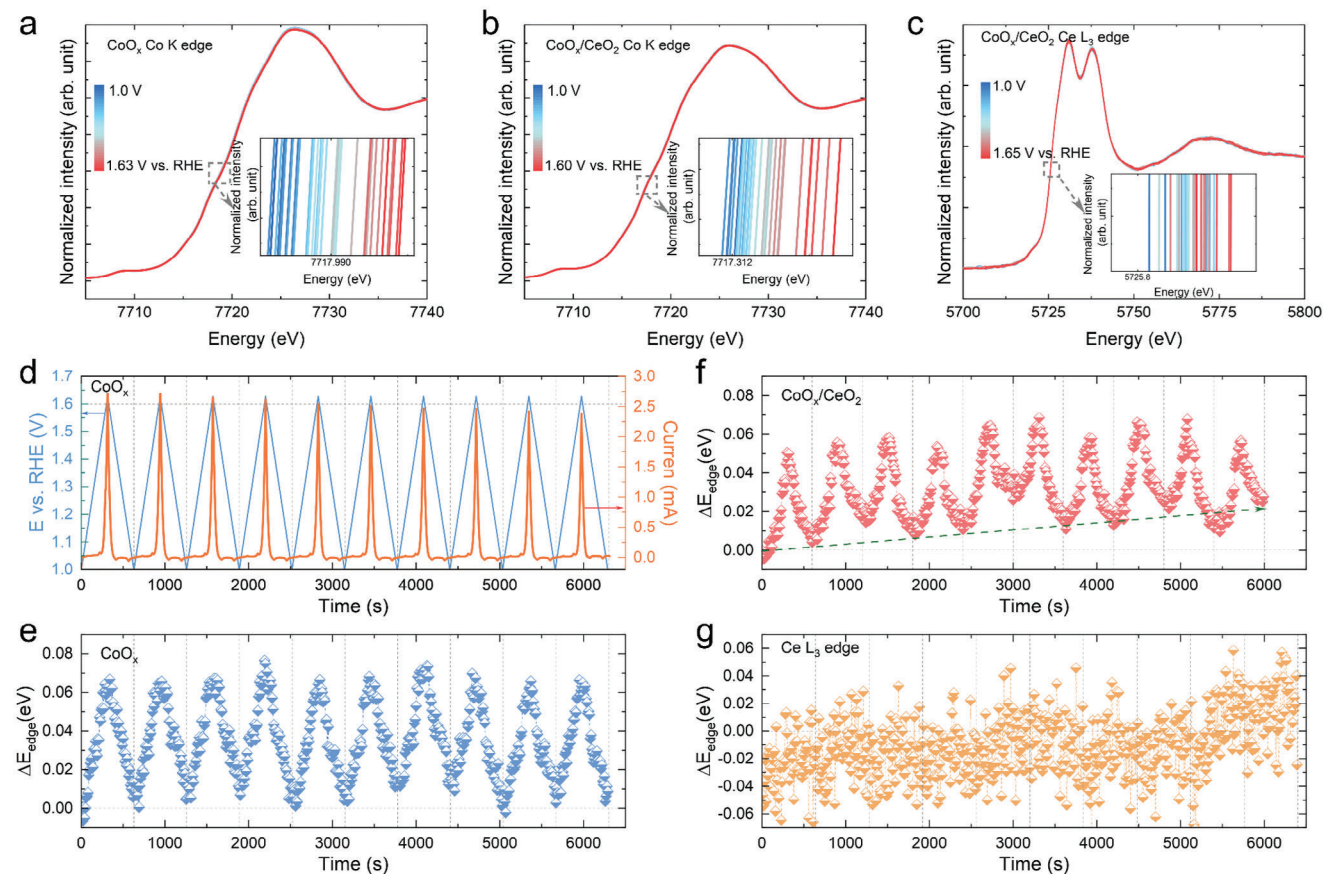


Figure 4. Operando hXAS characterizations on CoO_x and CoO_x/CeO₂ to monitor the evolution of Co K edge and Ce L₃ edge during CV measurement with a scan rate of 2 mV s⁻¹. The XANES spectra at the a) Co K edge of CoO_x, b) Co K edge of CoO_x/CeO₂ and c) Ce L₃ edge of CoO_x/CeO₂ during the first anodic scan. Insets in panel (a–c) highlights the shift in absorption edge. d) The applied potential and the OER current of CoO_x electrode as a function of time during the 10 CV cycles of the operando hXAS characterization. The corresponding energy shift (ΔE_{edge}) at the Co K edge spectra for e) CoO_x and f) CoO_x/CeO₂ during 10 CV cycles. g) The ΔE_{edge} at the Ce L₃ edge spectra for the CoO_x/CeO₂. The ΔE_{edge} in panel (e–g) was obtained by comparing the energy of absorption edge (E_{edge}) at the specific potential to that at 1.0 V versus RHE during first anodic scan.

of CoO_x/CeO₂ is ≈ 30 meV at ≈ 1.60 V versus RHE, that is, in the OER-region (Figure 5a), while for CoO_x is ≈ 60 meV consistently with the operando hXAS results observed during CV measurements (Figure 4d,e). The ΔE_{edge} for CoO_x/CeO₂ is also smaller than that of CoO_x at the same current value (Figure 5b). The variance in ΔE_{edge} thus Co oxidation state could alter both the interfacial capacitance and total charge on the electrode surface. To reveal the change in the interfacial capacitance, in situ impedance spectroscopy at different applied potentials (Figure S20, Supporting Information) was conducted to derive Mott–Schottky plots (Figure 5c). The negative slope indicates that CoO_x is p-type in nature,^[8c,21] in contrast to the CeO₂ reference (Figure S21, Supporting Information). The slope for CoO_x/CeO₂ is also negative, but is less steep than that of CoO_x, suggesting a higher electron hole concentration is present at the surface since this is inversely proportional to the gradient.^[22] Besides, the flat band potential (E_{fb}) was extracted from the intercept of the Mott–Schottky plots. The different E_{fb} of 1.32 V versus RHE for CoO_x/CeO₂ compared to that of CoO_x (1.15 V versus RHE) verifies the electronic modulation that arises from the addition of CeO₂ to CoO_x. More interestingly, the E_{fb} can have an impact on the evolution of the Co

oxidation state during OER. Indeed, theoretically electron holes can be generated with Co being oxidized and can accumulate in the space-charge region when the applied potential is higher than E_{fb} (inset in Figure 5c).^[23] This can explain why the ΔE_{edge} (see Figure 5a) increases after ≈ 1.15 V and 1.32 V versus RHE in CoO_x and CoO_x/CeO₂, respectively (i.e., after the E_{fb}).

Furthermore, a pulse voltammetry protocol^[24] (see Figures S22 and S23, Supporting Information, for more details) was used to reveal the total charge related to space charge region and electric double layer at the catalyst/electrolyte interface (Figure 5d). There is a linear relationship between the total charge and log (j), indicating that the generated current is controlled by the accumulated charge in the catalyst.^[24] The total charge in CoO_x at the same log (j) value is always higher than that of CoO_x/CeO₂, likely correlated to the higher ΔE_{edge} (i.e., Co oxidation) during OER for CoO_x compared to CoO_x/CeO₂ as observed by operando hXAS during CP (Figure 5b). Moreover, Figure 5b also shows that the ΔE_{edge} for CoO_x has stronger dependence on the log (j) in the OER region; by comparison, the ΔE_{edge} of CoO_x/CeO₂ is almost unchanged. These results suggest two catalysts may follow different reaction pathways during the OER.

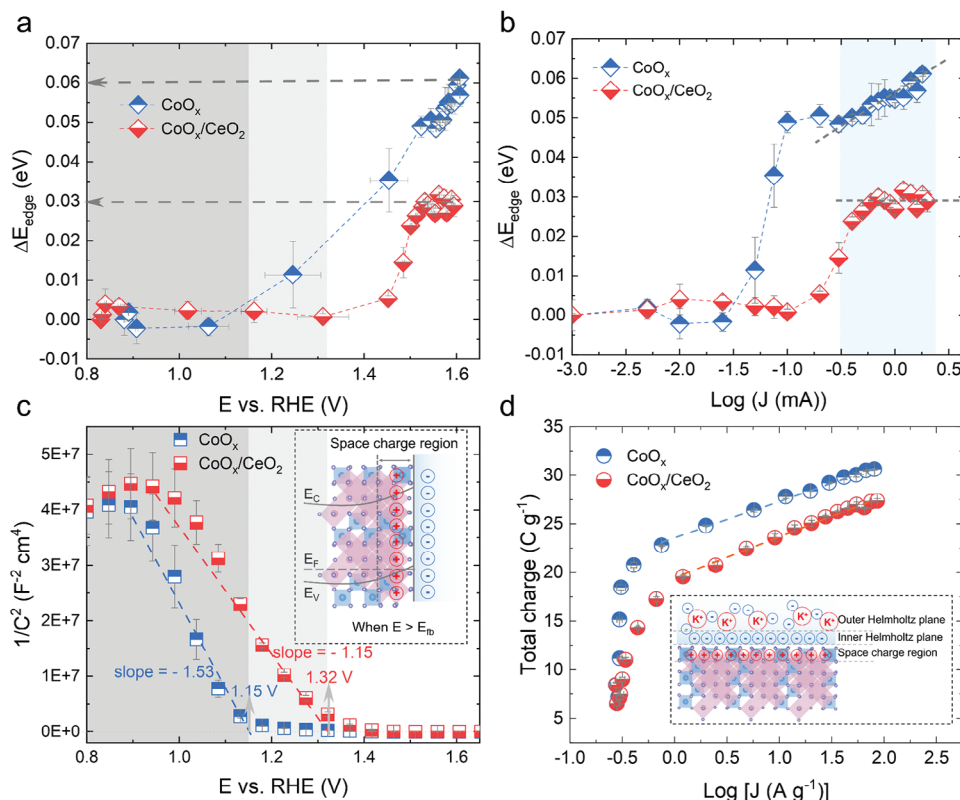


Figure 5. Correlations among Co oxidation state, electronic structures and surface charge in CoO_x and $\text{CoO}_x/\text{CeO}_2$. The ΔE_{edge} being plotted against the a) applied potential and b) $\log(j)$ that obtained during the steady-state CP measurement in a flow cell (Figure S18, Supporting Information). The ΔE_{edge} herein is calculated by comparing E_{edge} at different condition to that seen at the initial step with a constant current of 0.001 mA. c) Mott–Schottky plots to extract the E_{fb} ; inset shows the space charge region at the surface of the catalysts when the applied potential is higher than E_{fb} . d) Total charge at the catalyst/electrolyte surface as a function of $\log(j)$ that measured in the rotating disk electrode; inset shows the total charge accumulated at the space charge region and electric double layer. The error bars in this figure are from the averages on three data points.

To shed light on the reaction mechanism, a pH-dependence study was conducted. Tafel plots were made to compare the OER activity of CoO_x and $\text{CoO}_x/\text{CeO}_2$ in the electrolytes of different OH^- concentration, and their reaction order at 1.60 V versus RHE was determined to be ≈ 0.46 and 0.26, respectively (Figure 6a–c). A higher reaction order implies a stronger dependence of activity on pH, suggesting the proton (or OH^-) and electron transfer steps are decoupled during the rate-determining step (RDS).^[25] In contrast, pH-independent OER activity involves a concerted proton electron transfer (CPET) during the RDS. The reaction order of $\text{CoO}_x/\text{CeO}_2$ is lower than that of CoO_x , suggesting the RDS is more likely to be dominated by a CPET process.

In an alkaline environment, the pH-dependent activity is majorly controlled by the OH^- and/or electron transfer in the RDS. The participation of bridging oxygen (or lattice oxygen) in the OER has been frequently suggested for Co-based catalysts, generally in combination with pH-dependent OER activity in which OH^- and electron transfer are decoupled in the RDS.^[8a,b,25b] For example, the OER mechanism a Co–Ni–N–C catalyst developed by Bai et al. has been suggested to proceed via an electron transfer as the pre-equilibrium step, followed by an OH^- transfer as the RDS.^[10b] However, the OH^- and electron transfer could be still concerted even when followed by the lattice oxygen evolution reaction mechanism; the activation energy for the concerted

pathway may be even lower if there is no restriction on hydroxyl exchange.^[25c] Besides, Co^{IV} is widely accepted to be the key intermediate preceding the OER, and the O–O bond coupling is generally regarded as the RDS.^[10b,26]

Therefore, we propose two reaction pathways: one has a decoupled proton transfer as the RDS, while the other has a CPET as RDS. CoO_x shows no obvious peak for the protonated bridging oxygen in the O K edge spectra (Figure 3c); the ΔE_{edge} of the Co K edge shows stronger dependence on $\log(j)$ and is higher than that in $\text{CoO}_x/\text{CeO}_2$ (Figure 5b). Finally, CoO_x presents a reaction order of ≈ 0.46 . Consequently, we propose that CoO_x would largely follow the non-concerted reaction pathway (Figure 6d). The OER cycle may start with a decoupled electron transfer in $\text{Co}^{\text{III}}\text{—O—Co}^{\text{IV}}$ to form the Co^{IV} dimer, and then proceed with deprotonation via OH^- attack during the RDS. By comparison, the $\text{CoO}_x/\text{CeO}_2$ shows an obvious peak for the protonated bridging oxygen in the O K edge spectra (Figure 3d); the ΔE_{edge} of the Co K edge is both less dependence on $\log(j)$ and lower than that of CoO_x (Figure 5b). In addition, $\text{CoO}_x/\text{CeO}_2$ shows a small reaction order (≈ 0.26) suggesting that a CPET process likely dominates the RDS in $\text{CoO}_x/\text{CeO}_2$ (Figure 6e). The $\text{Co}^{\text{III}}\text{—OH—Co}^{\text{IV}}$, with protonated bridging oxygen, may proceed the O–O formation, via a one electron transfer process coupled with deprotonation by OH^- attack. In this mechanism, there is no need to form the

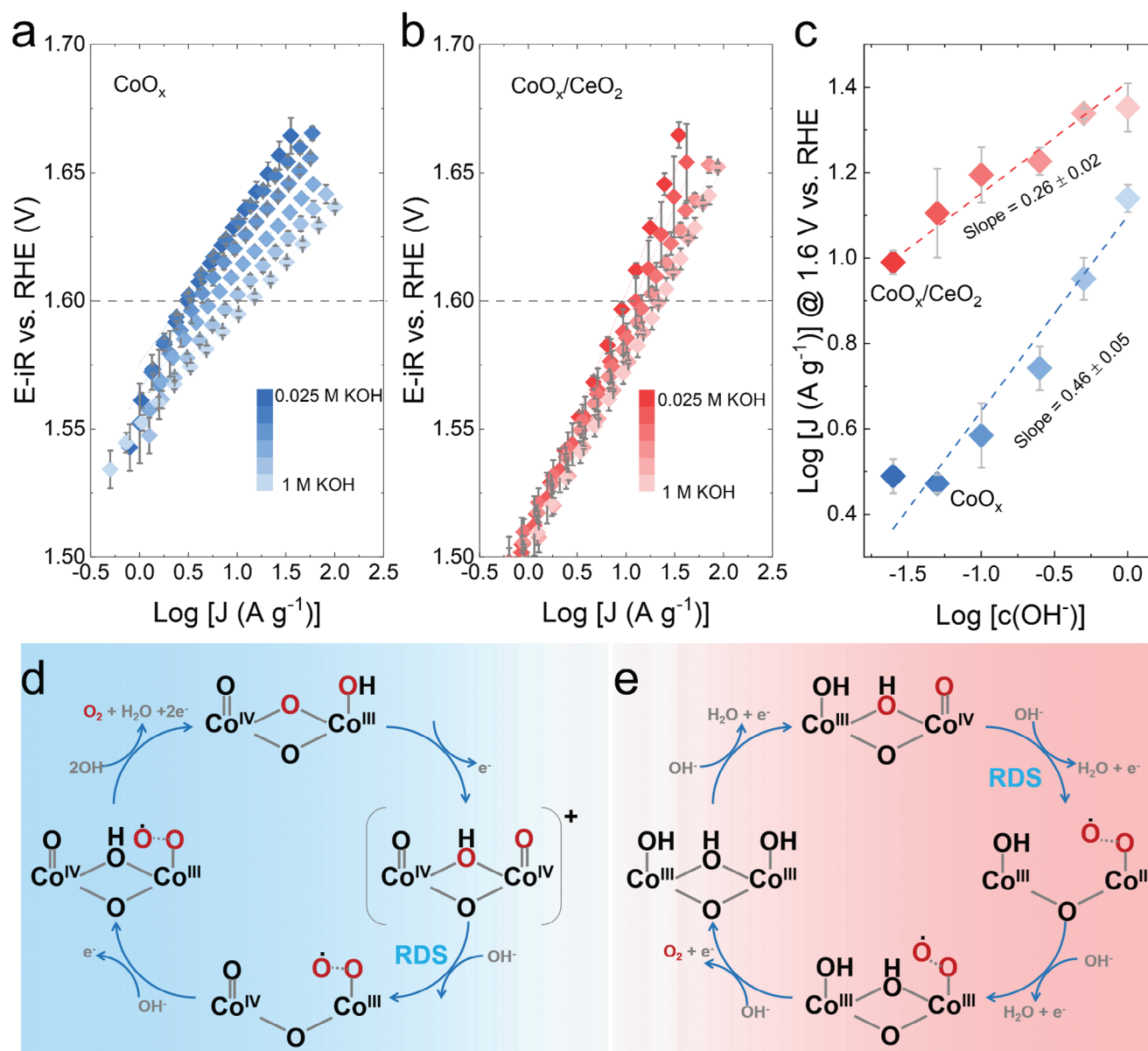


Figure 6. Reaction order and proposed reaction pathways. The pH-dependent Tafel plots of a) CoO_x and b) CoO_x/CeO₂. c) The log (J) at 1.6 V versus RHE was plotted against the log [c(OH)⁻] to extract the reaction order. The error bars are from the averages on three individual measurements. The proposed reaction pathways d) with chemical proton transfer as the RDS, or e) with concerted proton electron transfer during RDS. The oxygen that participated in the O—O bond formation is marked in red.

Co^{IV} dimer, which explains the lower ΔE_{edge} and its reduced dependence on log (J). Note that different reaction pathways could occur concurrently (and this is why we talk about a dominating mechanism) and there could be other possible reaction pathways, for instance involving a single Co as the active center (Figure S24, Supporting Information), or the direct O—O coupling in a Co^{IV} dimer without the participation of bridging oxygen (Figure S25, Supporting Information). We anticipate those pathways are not dominant in the two catalysts, since they cannot fully explain the reaction order and the trend of Co oxidation state changes during OER. In all, the two preferred reaction pathways are based on the outlined structural features and electronic transformations,

which demonstrate the different electrochemical properties of CoO_x and CoO_x/CeO₂. Evidently, though CeO₂ does not directly participate in the OER reaction mechanism, its electronic modulation effects can alter the CoO_x surface structure and Co redox properties to change the reaction mechanism and improve the OER activity of CoO_x.

3. Conclusion

In summary, the OER enhancement mechanisms of CoO_x/CeO₂ nanocomposite compared to CoO_x have been systematically revealed by combining ex situ/operando spectroscopic

characterizations with comprehensive electrochemical analyses. Introducing CeO₂ to CoO_x leads to a higher fraction of surface Co^{III} and protonated bridging oxygen, as evidenced by ex situ sXAS characterizations. With the help of operando hXAS characterizations, we showed that the evolution of the Co oxidation state was controlled by the E_{fb}. The E_{fb} is modulated by the introduction of CeO₂, thus, the CoO_x/CeO₂ shows different Co oxidation behavior with applied potential. The energy shift in the Co K edge of CoO_x/CeO₂ is less significant and less dependent on log (J) compared that of CoO_x. Besides, the CoO_x/CeO₂ has a smaller reaction order for OH[−] than that of CoO_x, as revealed by the pH-dependence study. Based on the spectroscopic characterizations and electrochemical analyses, we propose the RDS for the CoO_x/CeO₂ is dominated by a CPET process, with involvement of protonated bridging oxygen, in comparison to a non-concerted reaction pathway for CoO_x. Finally, we find that CeO₂ is not directly involved in the OER cycle, though it modifies the structural and electronic properties of CoO_x, changes the reaction pathway and improves the OER activity.

Supporting Information

Supporting Information is available from the Wiley Online Library or from the author.

Acknowledgements

The hXAS and sXAS characterizations were carried out in the SuperXAS X10DA beamline and Phoenix X07MB beamline respectively, at the Swiss Light Source, Paul Scherrer Institute, Villigen, Switzerland. E.F., J.H., and N.H. gratefully acknowledge the Swiss National Science Foundation through its PRIMA grant (grant no. PR00P2_193111) and the NCCR MARVEL, a National Centre of Competence in Research, funded by the Swiss National Science Foundation. TJS thanks the Swiss Center of Excellence for NetZero Emissions.

Open access funding provided by ETH-Bereich Forschungsanstalten.

Conflict of Interest

The authors declare no conflict of interest.

Data Availability Statement

The data that support the findings of this study are openly available in Materials Cloud at <https://doi.org/10.24435/materialscloud:yh-sq>, reference number 2023157.

Keywords

CeO₂, Co oxidation state, Co redox, operando XAS, oxygen evolution reaction

Received: October 18, 2023

Revised: January 22, 2024

Published online:

- [1] a) A. M. Oliveira, R. R. Beswick, Y. Yan, *Curr. Opin. Chem. Eng.* **2021**, 33, 100701; b) J. Chi, H. Yu, *Chin. J. Catal.* **2018**, 39, 390; c)

- M. J. O'Malley, M. B. Anwar, S. Heinen, T. Kober, J. McCalley, M. McPherson, M. Muratori, A. Orths, M. Ruth, T. J. Schmidt, A. Tuohy, *Proc. IEEE* **2020**, 108, 1437.
[2] a) T. Kou, S. Wang, Y. Li, *ACS Mater. Lett.* **2021**, 3, 224; b) D. Hua, J. Huang, E. Fabbri, M. Rafique, B. Song, *ChemElectroChem* **2022**, 10, 202200999.
[3] a) E. Fabbri, M. Nachtegaal, T. Binninger, X. Cheng, B. J. Kim, J. Durst, F. Bozza, T. Graule, R. Schaublin, L. Wiles, M. Pertoso, N. Danilovic, K. E. Ayers, T. J. Schmidt, *Nat. Mater.* **2017**, 16, 925; b) J. Song, C. Wei, Z. F. Huang, C. Liu, L. Zeng, X. Wang, Z. J. Xu, *Chem. Soc. Rev.* **2020**, 49, 2196; c) E. Marelli, J. Gazquez, E. Poghosyan, E. Muller, D. J. Gawryluk, E. Pomjakushina, D. Sheptyakov, C. Piamonteze, D. Aegerter, T. J. Schmidt, M. Medarde, E. Fabbri, *Angew. Chem., Int. Ed.* **2021**, 60, 14609.
[4] a) J. Huang, J. Han, R. Wang, Y. Zhang, X. Wang, X. Zhang, Z. Zhang, Y. Zhang, B. Song, S. Jin, *ACS Energy Lett.* **2018**, 3, 1698; b) Y. Zhu, W. Zhou, Z. Shao, *Small* **2017**, 13, 1603793.
[5] a) A. H. Clark, K. A. Beyer, S. Hayama, T. I. Hyde, G. Sankar, *Chem. Mater.* **2019**, 31, 7744; b) T. Montini, M. Melchionna, M. Monai, P. Fornasiero, *Chem. Rev.* **2016**, 116, 5987.
[6] a) J. Wang, X. Xiao, Y. Liu, K. Pan, H. Pang, S. Wei, *J. Mater. Chem. A* **2019**, 7, 17675; b) J. Huang, H. Sheng, R. D. Ross, J. Han, X. Wang, B. Song, S. Jin, *Nat. Commun.* **2021**, 12, 3036; c) K. Obata, K. Takanebe, *Angew. Chem., Int. Ed.* **2018**, 57, 1616; d) C. Song, Q. Zhan, F. Liu, C. Wang, H. Li, X. Wang, X. Guo, Y. Cheng, W. Sun, L. Wang, J. Qian, B. Pan, *Angew. Chem., Int. Ed.* **2022**, 61, 202200406.
[7] a) J.-H. Kim, K. Shin, K. Kawashima, D. H. Youn, J. Lin, T. E. Hong, Y. Liu, B. R. Wygant, J. Wang, G. Henkelman, C. B. Mullins, *ACS Catal.* **2018**, 8, 4257; b) B. Qiu, C. Wang, N. Zhang, L. Cai, Y. Xiong, Y. Chai, *ACS Catal.* **2019**, 9, 6484; c) Y. Liu, C. Ma, Q. Zhang, W. Wang, P. Pan, L. Gu, D. Xu, J. Bao, Z. Dai, *Adv. Mater.* **2019**, 31, 1900062; d) M. Li, X. Wang, K. Liu, H. Sun, D. Sun, K. Huang, Y. Tang, W. Xing, H. Li, G. Fu, *Adv. Mater.* **2023**, 35, 2302462.
[8] a) J. T. Mefford, X. Rong, A. M. Abakumov, W. G. Hardin, S. Dai, A. M. Kolpak, K. P. Johnston, K. J. Stevenson, *Nat. Commun.* **2016**, 7, 11053; b) Y. Pan, X. Xu, Y. Zhong, L. Ge, Y. Chen, J. M. Veder, D. Guan, R. O'Hayre, M. Li, G. Wang, H. Wang, W. Zhou, Z. Shao, *Nat. Commun.* **2020**, 2020, 11; c) X. Cheng, E. Fabbri, Y. Yamashita, I. E. Castelli, B. Kim, M. Uchida, R. Haumont, I. Puente-Orench, T. J. Schmidt, *ACS Catal.* **2018**, 8, 9567.
[9] H. Dau, P. Liebisch, M. Haumann, *Anal. Bioanal. Chem.* **2003**, 376, 562.
[10] a) A. L. Li, S. Kong, C. X. Guo, H. Ooka, K. Adachi, D. Hashizume, Q. K. Jiang, H. X. Han, J. P. Xiao, R. Nakamura, *Nat. Catal.* **2022**, 5, 109; b) L. Bai, C.-S. Hsu, D. T. L. Alexander, H. M. Chen, X. Hu, *Nat. Energy* **2021**, 6, 1054; c) I. Miyazato, L. Takahashi, K. Takahashi, *Mol. Syst. Des. Eng.* **2019**, 4, 1014.
[11] A. Bergmann, T. E. Jones, E. M. Moreno, D. Teschner, P. Chernev, M. Gliech, T. Reier, H. Dau, P. Strasser, *Nat. Catal.* **2018**, 1, 711.
[12] V. Pfeifer, T. E. Jones, J. J. Velasco Velez, R. Arrigo, S. Piccinin, M. Havecker, A. Knop-Gericke, R. Schlögl, *Chem. Sci.* **2017**, 8, 2143.
[13] S. Soni, M. Dave, B. Dalela, P. A. Alvi, S. Kumar, S. S. Sharma, D. M. Phase, M. Gupta, S. Dalela, *Appl. Phys. A* **2020**, 126, 585.
[14] Z. Xiao, Y. C. Huang, C. L. Dong, C. Xie, Z. Liu, S. Du, W. Chen, D. Yan, L. Tao, Z. Shu, G. Zhang, H. Duan, Y. Wang, Y. Zou, R. Chen, S. Wang, *J. Am. Chem. Soc.* **2020**, 142, 12087.
[15] M. Li, X. Wang, K. Liu, H. Sun, D. Sun, K. Huang, Y. Tang, W. Xing, H. Li, G. Fu, *Adv. Mater.* **2023**, 35, 2302462.
[16] X. Cheng, E. Fabbri, M. Nachtegaal, I. E. Castelli, M. El Kazzi, R. Haumont, N. Marzari, T. J. Schmidt, *Chem. Mater.* **2015**, 27, 7662.
[17] W. Q. Guo, H. L. Luo, D. X. Fang, Z. Jiang, J. S. Chi, W. F. Shangguang, *J. Energy Chem.* **2022**, 70, 373.
[18] a) R. Zhang, N. Dubouis, M. Ben Osman, W. Yin, M. T. Sougrati, D. A. D. Corte, D. Giaume, A. Grimaud, *Angew. Chem., Int. Ed.* **2019**,

- 58, 4571; b) E. B. Isaacs, S. Sharifzadeh, B. Ma, J. B. Neaton, *J. Phys. Chem. Lett.* **2011**, 2, 2531.
- [19] T. Wu, S. Sun, J. Song, S. Xi, Y. Du, B. Chen, W. A. Sasangka, H. Liao, C. L. Gan, G. G. Scherer, L. Zeng, H. Wang, H. Li, A. Grimaud, Z. J. Xu, *Nat. Catal.* **2019**, 2, 763.
- [20] L. Bai, C. S. Hsu, D. T. L. Alexander, H. M. Chen, X. Hu, *J. Am. Chem. Soc.* **2019**, 141, 14190.
- [21] R. Wang, J. Han, P. Xu, T. Gao, J. Zhong, X. Wang, X. Zhang, Z. Li, L. Xu, B. Song, *Adv. Sci.* **2020**, 7, 2000216.
- [22] S. P. Harrington, T. M. Devine, *J. Electrochem. Soc.* **2008**, 155, C381.
- [23] A. W. Bott, *Curr. Sep.* **1998**, 17, 87.
- [24] H. N. Nong, L. J. Falling, A. Bergmann, M. Klingenhof, H. P. Tran, C. Spori, R. Mom, J. Timoshenko, G. Zichittella, A. Knop-Gericke, S. Piccinin, J. Perez-Ramirez, B. R. Cuenya, R. Schlogl, P. Strasser, D. Teschner, T. E. Jones, *Nature* **2020**, 587, 408.
- [25] a) L. Giordano, B. Han, M. Risch, W. T. Hong, R. R. Rao, K. A. Stoerzinger, Y. Shao-Horn, *Catal. Today* **2016**, 262, 2; b) A. Grimaud, O. Diaz-Morales, B. Han, W. T. Hong, Y.-L. Lee, L. Giordano, K. A. Stoerzinger, M. T. M. Koper, Y. Shao-Horn, *Nat. Chem.* **2017**, 9, 457; c) Z.-F. Huang, J. Song, Y. Du, S. Xi, S. Dou, J. M. V. Nsanzimana, C. Wang, Z. J. Xu, X. Wang, *Nat. Energy* **2019**, 4, 329.
- [26] a) J. B. Gerken, J. G. McAlpin, J. Y. C. Chen, M. L. Rigsby, W. H. Casey, R. D. Britt, S. S. Stahl, *J. Am. Chem. Soc.* **2011**, 133, 14431; b) H. Yang, F. S. Li, S. Q. Zhan, Y. W. Liu, W. L. Li, Q. J. Meng, A. Kravchenko, T. Q. Liu, Y. Yang, Y. Fang, L. Q. Wang, J. Q. Guan, I. Furo, M. S. G. Ahlquist, L. C. Sun, *Nat. Catal.* **2022**, 5, 414; c) C. Pasquini, I. Zaharieva, D. Gonzalez-Flores, P. Chernev, M. R. Mohammadi, L. Guidoni, R. D. L. Smith, H. Dau, *J. Am. Chem. Soc.* **2019**, 141, 2938; d) G. Mattioli, P. Giannozzi, A. Amore Bonapasta, L. Guidoni, *J. Am. Chem. Soc.* **2013**, 135, 15353.